

# Weak Localization in Mono-layer Graphene with Rashba Spin-Orbit Interaction

Eduardo Serna\*

*Centro de Investigación en Ciencias, Universidad Autónoma del Estado de Morelos, Morelos, 62209, México*

I. Rodríguez Vargas†

*Unidad Académica de Física, Universidad Autónoma de Zacatecas, Zacatecas, 98060, México*

L. Diago-Cisneros‡

*Facultad de Física, Universidad de La Habana, La Habana, 10400, Cuba*

(Dated: 26 December 2024)

This paper presents a theoretical and computational study on the impact of Rashba spin-orbit interaction (SOIR) on electron transmission through a potential barrier in monolayer graphene. The energy dispersion relations were numerically obtained via the finite differences method applied to the Schrödinger equation, using a model Hamiltonian incorporating graphene, SOIR, and a potential barrier. Our findings reveal that the presence of SOIR significantly modifies the electron transmission coefficients compared with pristine graphene conditions. While electron transmission in pristine graphene remains near unity with minor reductions due to quantum interference effects in a Gaussian wave packet, introducing SOIR leads to intricate transmission patterns dependent on the barrier parameters and wave packet characteristics. These effects arise from phenomena such as spin degeneracy lifting and spin-dependent scattering mechanisms. The results emphasize the critical role that SOIR plays in engineering sophisticated quantum devices, offering potential applications in spintronic technologies and quantum computing.

## I. INTRODUCTION

Understanding quantum dispersion in graphene, the correlation between energy levels and corresponding wave vectors, is crucial for unveiling graphene's remarkable electronic and transport properties.

Graphene's distinctive two-dimensional honeycomb lattice structure leads to linear dispersion around the Dirac points. This results in massless Dirac fermions that display remarkable properties, including extremely high carrier mobility, ballistic transport across distances of several microns, and the lack of a bandgap in pristine graphene sheets[1]. Insights into quantum dispersion are imperative not only for elucidating these intrinsic electronic characteristics but also for exploring

quantum phenomena such as weak localization, spin-orbit interactions, and topologically protected quantum phases. These quantum effects form the foundation of advanced technological developments, particularly in areas like spintronics and quantum computing[2–4]. To accurately investigate and simulate the dynamics of charge carriers in graphene, the Schrödinger equation serves as a fundamental tool. As quantum mechanics dictate electron behavior at atomic scales, solving this equation provides crucial insights into energy-momentum relationships and quantum mechanical characteristics of electron transport. Moreover, accounting precisely for spin-related phenomena and spatial quantum interference effects requires analytically or numerically solving the Schrödinger equation under relevant physical conditions. Numerically, solving the Schrödinger equation frequently requires robust computational approaches. One prominent numerical method is the finite differences method (FDM), a discretization technique used to approximate continuous differential operators as algebraic equations solved computationally. FDM is particularly helpful due to its simplicity, computational efficiency, and versatility in handling complex boundary and potential configurations encountered in structural graphene studies-making it particularly suited for calculating electronic properties and energy dispersion relations. The primary objective of this work is to derive and numerically compute the energy dispersion relations for monolayer graphene, using the finite differences method applied to the Schrödinger equation. Specifically, this involves defining the model Hamiltonian representing charge carrier dynamics, discretizing the governing equations via FDM, and computationally obtaining dispersion curves. An accurate prediction of these energy dispersion relations provides essential insights into graphene's charge carrier dynamics and establishes a foundational knowledge base for engineering graphene-based materials and devices tailored to advanced electronic and spintronic applications.

---

\* sernaed95@gmail.com

† isaac@fisica.uaz.edu.mx

‡ ldiago@fisica.uh.cu

## A. Rashba-Type Spin-Orbit Interaction

Applying an electrostatic potential to graphene can create regions where electrons are classically forbidden due to energy constraints[5]. For instance, a negative gate voltage can shift the Fermi level into the valence band, establishing a potential barrier that electrons do not have sufficient energy to overcome, according to classical physics[6]. However, in graphene, electron transmission through such barriers can exhibit unusual behavior due to the Klein paradox.

The Klein paradox describes the phenomenon where electrons in graphene can tunnel through electrostatic potential barriers with a probability approaching unity, even at perpendicular incidence, seemingly defying the principles of classical mechanics[7]. This counterintuitive transmission arises from the relativistic nature of electrons in graphene, where, within the barrier region, incident electrons can be converted into holes, allowing for unimpeded passage[8]. The Klein paradox is a direct consequence of graphene's unique linear dispersion relation and the associated massless Dirac fermion behavior. While this perfect transmission through barriers might pose challenges for achieving electron confinement in some device designs, it also presents opportunities for developing novel tunneling-based electronic devices. Beyond simply creating a forbidden region, the application of electrostatic potential can dramatically alter electron transmission through various other mechanisms, influencing the refractive index and leading to phenomena like electron lensing[9].

Rashba spin-orbit interaction (RSOI) is a relativistic effect that arises in systems lacking structural inversion symmetry[10]. In graphene, RSOI can be induced by an external electric field applied perpendicular to the graphene plane or through proximity to a substrate[11]. A key consequence of RSOI is the breaking of spin degeneracy, where the energy levels of electrons with opposite spins are no longer the same, even in the absence of an external magnetic field[12]. Controlling spin degeneracy through electric fields via Rashba spin-orbit interaction (RSOI) is particularly valuable for spintronic applications. It enables electron spin manipulation without depending on magnetic fields, which typically require more power and are challenging to incorporate effectively into nanoscale systems.

Furthermore, RSOI modifies the effective mass of charge carriers in graphene. It can lead to the opening of an energy gap at the Dirac points, effectively giving the otherwise massless Dirac fermions a finite mass. In systems with strong spin-orbit coupling, such as certain heavy-hole systems, specific types of RSOI (like  $k^3$ -Rashba spin-orbit coupling) can even result in anisotropic band structures and the emergence of additional spin-degeneracy points under light illumination. While this specific example refers to heavy holes, the principle that RSOI can significantly alter the band structure and effective mass of carriers is relevant to graphene, partic-

ularly when considering proximity-induced effects from substrates with strong spin-orbit coupling[13]. The modification of the effective mass by RSOI can profoundly impact graphene's transport properties, influencing carrier mobility and the density of states. Notably, tuning the strength of RSOI in graphene can even induce a transition from the Klein tunneling regime (perfect transmission) to the anti-Klein tunneling regime (perfect reflection) when electrons encounter a potential barrier. This ability to control the transmission probability through potential barriers using RSOI opens up exciting possibilities for creating novel electronic devices that leverage this fundamental quantum mechanical phenomenon[14].

## II. DEVELOPMENT

### A. Physical Model

A quantum channel was fabricated using a hexagonal boron nitride substrate, upon which monolayer graphene (MLG) was deposited and subsequently capped with a silicon dioxide layer. Two metallic electrodes were incorporated to generate a perpendicular electric field, thereby confining a Gaussian wave packet (GWP) within the graphene. We also added a rectangular electrostatic potential barrier, where we incorporate the Rashba-type spin-orbit interaction. The system is more deeply explained in our previous article[1]

### B. Mathematical Model

From the physical model, we can get a mathematical model which describes the temporal evolution and consequently the quantum dispersion of the fDs in the MLG.

Starting with the pristine graphene hamiltonian[15]:

$$\hat{H}_G = v_F \vec{\sigma} \cdot \vec{p}, \quad (1)$$

With  $\vec{\sigma} = \hat{\sigma}_x \hat{i} + \hat{\sigma}_y \hat{j}$ , being the pseudospin Pauli matrices  $\hat{\sigma}_x = \begin{pmatrix} 0 & 1 \\ 1 & 0 \end{pmatrix}$ ,  $\hat{\sigma}_y = \begin{pmatrix} 0 & -i \\ i & 0 \end{pmatrix}$ , and  $\vec{p} = \hat{p}_x \hat{i} + \hat{p}_y \hat{j}$ , the momentum operator, which  $x, y$  components read  $\hat{p}_x = -i\hbar \frac{\partial}{\partial x}$  and  $\hat{p}_y = -i\hbar \frac{\partial}{\partial y}$ , respectively. From this point forward,  $v_F$  stands for the Fermi velocity of the carriers in MLG, which satisfies

$$v_F \approx \frac{c}{300}. \quad (2)$$

The previous hamiltonian can be rewritten as:

$$\hat{H}_G = -i\hbar v_F \begin{pmatrix} 0 & \frac{\partial}{\partial x} - i \frac{\partial}{\partial y} \\ \frac{\partial}{\partial x} + i \frac{\partial}{\partial y} & 0 \end{pmatrix}. \quad (3)$$

Assuming that the momentum-dependent term of the Rashba Hamiltonian for Q1D (quasi-one dimensional)

semiconductor hetero-structures can be extended to the context of MLG-Q1D[1, 16], it follows that the hamiltonian for the SOIR can be written as:

$$\hat{H}_R = \begin{pmatrix} 0 & k_{\alpha-} + k_{\beta-} \\ k_{\alpha+} + k_{\beta+} & 0 \end{pmatrix}, \quad (4)$$

Where  $k_{\alpha\pm} = \alpha (k_{\pm}^2/k_{\mp})$  and  $k_{\beta\pm} = \beta k_{\pm}^3$ ; also defining that  $k_{\pm} = k_x \pm ik_y$  which are the initial wave numbers of the system. The symbols  $\alpha$  and  $\beta$  represent the linear and cubic contribution of the SOIR respectively. We are also taking into account that  $\alpha = -\beta$ , following the conclusions presented by Wong and Mireles[17].

For this research, we assume the heavy holes only in the region defined by the potential barrier.

The potential barrier is defined only in the specified region.

With the following hamiltonian:

$$\hat{H}_V = I_2 V(x) \quad (5)$$

Adding up the graphene(3), the SOIR(4), and the potential barrier(5) Hamiltonians, while also zeroing the parameters in the  $y$  direction, we get:

$$\hat{H} = \begin{pmatrix} V(x) & (k_{\alpha-} + k_{\beta-}) - i\hbar v_F \frac{\partial}{\partial x} \\ (k_{\alpha+} + k_{\beta+}) - i\hbar v_F \frac{\partial}{\partial x} & V(x) \end{pmatrix}. \quad (6)$$

Note that if we wanted to see the results in the  $y$  direction, we would have to zero the partial derivatives of  $x$ .

### C. Finite differences scheme

La principal ecuación a resolver es la ecuación de Schrödinger dependiente del tiempo:

$$i\hbar \frac{d}{dt} \Psi(x, t) = \hat{H} \Psi(x, t) \quad (7)$$

En nuestro caso consideramos un paquete de ondas gaussiano (GWP) para cada componente del pseudoespinor  $\Psi(x, t) = \begin{pmatrix} \psi_A(x, t) \\ \psi_B(x, t) \end{pmatrix}$ . El GWP en un tiempo inicial tiene la siguiente forma:

$$\psi_j(x, t_0) = \frac{\xi_j}{\sqrt{4\pi\sigma^2}} e^{-\frac{(x-x_0)^2}{2\sigma^2}} e^{ixk_0} \quad (8)$$

Donde  $\xi$  es la configuración inicial del pseudoespinor,  $k_0$  es el número de onda inicial en  $x$  y el subíndice  $j$  indica la componente que se está usando.

Para el desarrollo de este artículo estamos ocupando las siguientes opciones de configuración del pseudoespinor:

$$\xi = \begin{pmatrix} 1 \\ 0 \end{pmatrix}, \begin{pmatrix} 1 \\ 1 \end{pmatrix}, \begin{pmatrix} 1 \\ i \end{pmatrix}, \begin{pmatrix} 1 \\ e^{i\pi/4} \end{pmatrix}. \quad (9)$$

El paquete de ondas entonces queda definido de la siguiente manera:

$$\Psi(x, 0) = \frac{1}{\sqrt{\xi_A^2 + \xi_B^2}} \begin{pmatrix} \psi_A \\ \psi_B \end{pmatrix} \quad (10)$$

Para la densidad de probabilidad calculada a continuación, usamos la siguiente definición:

$$\rho(x, t) = |\Psi|^2 = |\psi_A|^2 + |\psi_B|^2 \quad (11)$$

### D. Temporal Evolution Operator

Para resolver la ecuación de Schrödinger(7) se propone el uso de un operador de evolución temporal(TEO), a partir de la siguiente ecuación:

$$\Psi(x, t) = \hat{U}(t, t_0) \Psi(x, t_0) \quad (12)$$

Podemos ver que al aplicar el operador, obtenemos un tiempo  $t$  para un tiempo  $t_0$ . Si se sustituye la ecuación del TEO(12) en la ecuación de Schrödinger(7), se puede desarrollar el álgebra y resolver la ecuación diferencial obteniendo al TEO. Sabemos que el hamiltoniano no depende del tiempo, entonces podemos reescribir la ec.(12) como:

$$\Psi(x, t) = e^{-\frac{i\delta t}{\hbar} \hat{H}} \Psi(x, t_0) \quad (13)$$

Donde  $\delta t$  es el paso en el tiempo que discretizaremos más adelante. La exponencial anterior se puede aproximar a través de la serie de Taylor de primer orden como:

$$e^{-\frac{i\delta t}{\hbar} \hat{H}} = \frac{2}{I + \frac{i\delta t}{2\hbar} \hat{H}} - bnI \quad (14)$$

Haciendo uso de un cambio de variable podemos reescribir la ecuación anterior(14) como:

$$\Phi(x, t_0) + \frac{i\delta t}{2\hbar} \hat{H} \Phi(x, t_0) = 2\Psi(x, t_0) \quad (15)$$

Esta ecuación representa un sistema de ecuaciones de  $2 \times 2$  (ya que tenemos dos incógnitas que son  $\phi_A$  y  $\phi_B$  y al desarrollar la matriz, podemos ver que se forman dos ecuaciones).

Como ambas ecuaciones tienen derivadas, ocupamos el método de diferencias finitas para resolver ambas ecuaciones para todo el espacio simultáneamente. Para realizar esto, primero discretizamos al sistema de ecuaciones(15) a lo largo de todo el espacio  $j$  desde 0 hasta  $J$ .

Para mantener la estabilidad del análisis numérico en el método de diferencias finitas, se debe respetar la siguiente condición[18]:

$$\delta t \leq \frac{(\delta x)^2}{2} \quad (16)$$

Para discretizar las derivadas, ocupamos la expansión en serie de Taylor hasta el primer grado para el punto  $x_j$  posterior y anterior:

$$\begin{aligned} f(x_j + \delta x) &= f(x_j) + (x_j + \delta x - x_j)f'(x_j) \\ &= f(x_j) + \delta x f'(x_j), \\ f(x_j - \delta x) &= f(x_j) + (x_j - \delta x - x_j)f'(x_j) \\ &= f(x_j) - \delta x f'(x_j) \end{aligned} \quad (17)$$

Si restamos la segunda ecuación de la primera y despejamos, podemos encontrar las “Diferencias Centradas” que podemos discretizar también como:

$$f'(x_j) = \frac{f(x_j + \delta x) - f(x_j - \delta x)}{2\delta x} = \frac{f_{j+1} - f_{j-1}}{2\delta x} \quad (18)$$

De este modo podemos reescribir nuestro sistema de ecuaciones, una vez realizada la discretización y el desarrollo algebraico de la matriz:

$$\phi_{A,j} + \frac{i\delta t}{2\hbar} (V_j \phi_{A,j} + (k_{\alpha-,j} + k_{\beta-,j}) \phi_{B,j} - i\hbar v_F \frac{\phi_{B,j+1} - \phi_{B,j-1}}{2\delta x}) = 2\psi_{A,j} \quad (19)$$

$$\phi_{B,j} + \frac{i\delta t}{2\hbar} (V_j \phi_{B,j} + (k_{\alpha+,j} + k_{\beta+,j}) \phi_{A,j} - i\hbar v_F \frac{\phi_{A,j+1} - \phi_{A,j-1}}{2\delta x}) = 2\psi_{B,j} \quad (20)$$

Si sumamos las ecuaciones ec.(19) y ec.(20):

$$2 \begin{pmatrix} \psi_{A,1} + \psi_{B,1} \\ \psi_{A,2} + \psi_{B,2} \\ \vdots \\ \psi_{A,J} + \psi_{B,J} \end{pmatrix} = \begin{pmatrix} N & Q & 0 & \dots & \dots & \dots & 0 \\ -Q & N & Q & 0 & \dots & \dots & 0 \\ 0 & -Q & N & Q & 0 & \dots & 0 \\ \vdots & 0 & -Q & N & Q & \ddots & 0 \\ \vdots & \vdots & 0 & -Q & N & \ddots & 0 \\ \vdots & \vdots & \vdots & \ddots & \ddots & \ddots & Q \\ 0 & 0 & 0 & 0 & 0 & -Q & N \end{pmatrix} \begin{pmatrix} \phi_{A,1} \\ \phi_{A,2} \\ \vdots \\ \phi_{A,J} \end{pmatrix} \quad (21)$$

$$+ \begin{pmatrix} M & Q & 0 & \dots & \dots & \dots & 0 \\ -Q & M & Q & 0 & \dots & \dots & 0 \\ 0 & -Q & M & Q & 0 & \dots & 0 \\ \vdots & 0 & -Q & M & Q & \ddots & 0 \\ \vdots & \vdots & 0 & -Q & M & \ddots & 0 \\ \vdots & \vdots & \vdots & \ddots & \ddots & \ddots & Q \\ 0 & 0 & 0 & 0 & 0 & -Q & M \end{pmatrix} \begin{pmatrix} \phi_{B,1} \\ \phi_{B,2} \\ \vdots \\ \phi_{B,J} \end{pmatrix} \quad (22)$$

Donde  $N = 1 + \frac{i\delta t}{2\hbar} (V_j + (k_{\alpha+,j} + k_{\beta+,j}))$ ,  $Q = \frac{i\hbar v_F}{2\delta x}$  y  $M = 1 + \frac{i\delta t}{2\hbar} (V_j + (k_{\alpha-,j} + k_{\beta-,j}))$ .

Como se puede ver, el tamaño de la matriz depende del tamaño de nuestro sistema. Si se escoge  $\delta x = 1\text{\AA}$  entonces un pozo cuántico de  $1200\text{\AA}$  generará una matriz de  $1200 \times 1200$ .

Repetimos el procedimiento anterior pero ahora restando las ecuaciones ec.(19) y ec.(20)

Viendo estas matrices podemos redefinirlas como dos

ecuaciones matriciales sencillas  $2\psi_+ = \mathbb{N}\phi_A + \mathbb{M}\phi_B$  y  $2\psi_- = \mathbb{L}\phi_A + \mathbb{P}\phi_B$ . Estas ecuaciones se pueden tratar como un sistema de ecuaciones matriciales que se resuelven así:

$$\begin{aligned} \phi_A &= (2\mathbb{N}^{-1})\psi_+ - (\mathbb{N}^{-1}\mathbb{M})\phi_B \\ \phi_B &= 2(-\mathbb{L}\mathbb{N}^{-1}\mathbb{M} + \mathbb{P})^{-1}(\psi_- - \mathbb{L}\mathbb{N}^{-1}\psi_+) \end{aligned} \quad (23)$$

Una vez que contamos con el sistema de ecuaciones

discretizado, se puede calcular la evolución temporal con:

$$\Psi_j^n + 1 = \Phi_j^n - \Psi_j^n \quad (24)$$

Repetiendo el proceso para cada  $n$  hasta llegar a  $N$ .

### E. Probability Current Density

Una vez que se cuenta con la evolución temporal, podemos calcular su coeficiente de transmisión a partir del cálculo de la corriente de densidad de probabilidad (PCD). Para encontrar esta corriente, partimos desde la siguiente ecuación de continuidad:

$$\frac{\partial \rho}{\partial t} + \nabla \cdot \vec{j} = 0 \quad (25)$$

Aplicando el traspuesto conjugado a la ecuación de Schrödinger dependiente del tiempo(7), y multiplicando por la derecha por  $\Psi$ ; lo podemos incorporar la ecuación de la densidad de probabilidad(11). Al mismo tiempo se considera el Hamiltoniano del grafeno(1), el cual sabemos que es hermitiano ya que se compone de las matrices de Pauli. De esta forma podemos construir la siguiente ecuación:

$$\frac{\partial}{\partial t} \int \rho d\vec{r} = -v_f \int (\Psi \vec{\sigma} \cdot \nabla \Psi^{T*} + \Psi^{T*} \vec{\sigma} \cdot \nabla \Psi) d\vec{r} \quad (26)$$

Podemos reescribir la ecuación factorizando  $\nabla$  y quitando la integral de ambos lados:

$$\frac{\partial}{\partial t} \rho = -v_f \nabla \cdot (\Psi^\dagger \vec{\sigma} \Psi) \quad (27)$$

Sustituyendo en la ecuación de continuidad de la densidad de probabilidad ec.(25):

$$\nabla \cdot \vec{j} = v_f \nabla \cdot (\Psi^\dagger \vec{\sigma} \Psi) \quad (28)$$

Eliminando  $\nabla$  de ambos lados:

$$\vec{j} = v_f \Psi^\dagger \vec{\sigma} \Psi \quad (29)$$

De esta forma, hemos obtenido la densidad de corriente de probabilidad en grafeno.

Si queremos obtener las componentes de la densidad de corriente, podemos hacerlo de la siguiente forma:

$$\vec{j} = v_f \begin{pmatrix} \Psi^\dagger \sigma_x \Psi \\ \Psi^\dagger \sigma_y \Psi \end{pmatrix} = v_f \begin{pmatrix} \Psi_A^\dagger \Psi_B + \Psi_B^\dagger \Psi_A \\ i(-\Psi_A^\dagger \Psi_B + \Psi_B^\dagger \Psi_A) \end{pmatrix} \quad (30)$$

To determine the numerical value of  $\vec{j}$ , we identify the peaks in the probability density plots. Subsequently, we

calculate the minima of the Gaussian curves to find the apparent width of the GWP. Finally, we locate two precise moments: immediately before the wave packet interacts with the potential barrier and the exact moment it has traversed the barrier.

Con los tiempos definidos de entrada ( $t_1$ ) y de salida ( $t_2$ ), usamos la ecuación ec.(30) para todo el espacio en cada uno de los tiempos.

Con esto podemos ahora sí calcular el coeficiente de transmisión:

$$T = \left| \frac{\vec{j}_{out} \cdot \hat{n}}{\vec{j}_{in} \cdot \hat{n}} \right|, \quad (31)$$

En este contexto, se realiza el cociente entre la corriente transmitida y la corriente incidente, considerando el producto con el vector normal a la barrera. En el caso unidimensional aquí abordado, dicho vector puede representarse como  $(1, 0)$  o  $(0, 1)$ , dependiendo de si el paquete de onda gaussiano (GWP) se propaga a lo largo del eje  $x$  o del eje  $y$ , respectivamente.

### III. DISCUSSION OF RESULTS

A continuación se muestran las figuras obtenidas con el procedimiento obtenido anteriormente.

En las imágenes podemos notar ciertos aspectos interesantes, empezando con la fig.1. La imagen presenta dos gráficos que ilustran el coeficiente de transmisión ( $T$ ) en función de  $Vb$  (en meV) y  $k_0$  (en  $\text{\AA}^{-1}$ ) para un valor fijo de  $\xi = (1, 0)$ . El gráfico de la izquierda es una visualización tridimensional donde  $T$  está en el eje  $z$ ,  $Vb$  en el eje  $x$  y  $k_0$  en el eje  $y$ , con una escala de colores que varía desde morado oscuro (menor  $T$ ) hasta amarillo brillante (mayor  $T$ ). El gráfico de la derecha es un mapa de calor bidimensional que ofrece una vista superior, con el eje  $x$  representando  $k_0$  y el eje  $y$  representando  $Vb$ , usando el mismo mapa de colores que el gráfico 3D. Ambos gráficos muestran que el coeficiente de transmisión generalmente se mantiene muy cerca de 1, indicando una alta transmisión. Conforme aumenta  $Vb$ ,  $T$  tiende a disminuir, mientras que la dependencia respecto a  $k_0$  es mínima. En general, los gráficos demuestran cómo cambia  $T$  con variaciones en  $Vb$  y  $k_0$ , destacando una leve disminución de  $T$  al aumentar  $Vb$  y un cambio insignificante respecto a  $k_0$ .

Este resultado muestra una contradicción con lo que ya se especifica en la literatura, en el grafeno se esperaría observar una transmisión total debido a las mismas propiedades del material[19, 20].

The previously described behavior might be the result of one or both of the following aspects:

- **Wave Packet Characteristics:** Not a single momentum eigenstate. Debido a que estamos ocupando paquetes de onda en la simulación, un detalle importante que surge es que existe la presencia de

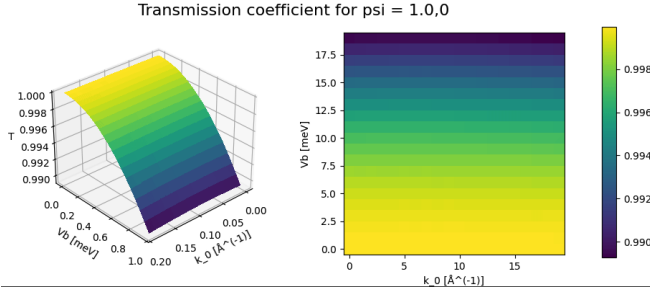


FIG. 1: Transmission coefficient ( $T$ ) in pristine graphene with initial pseudospin configuration  $\xi = (1, 0)$ , plotted against potential barrier height ( $Vb$ , in meV) and initial wave vector ( $k_0$ , in  $\text{\AA}^{-1}$ ). The 3D plot and 2D heatmap show that transmission is largely independent of the initial wave vector but decreases noticeably as the barrier height increases, ranging from 1 to approximately 0.990.

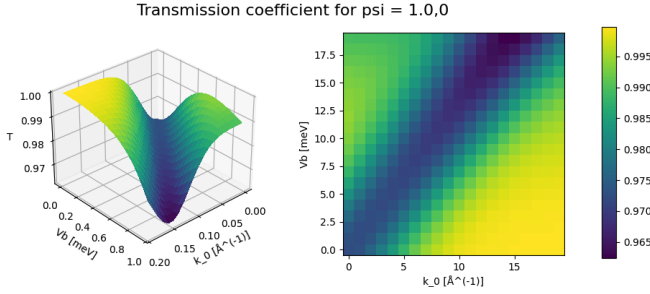


FIG. 2: Coeficiente de transmisión ( $T$ ) en función de la altura de la barrera de potencial ( $Vb$ ) y el número de onda inicial ( $k_0$ ) con una configuración inicial de pseudospin  $\xi = (1, 0)$ . La superficie 3D y el mapa de color 2D muestran una dependencia no monótona de  $T$  con respecto a  $Vb$  y  $k_0$ , destacando la influencia del acoplamiento espín-órbita en la transmisión a través de la barrera.

múltiples componentes de momentum y eso implica que algunos de ellos pueden causar interferencia con otros; causando un coeficiente de transmisión que difiere del de un solo autoestado[21]. Además, en nuestra simulación se está tomando en cuenta el tiempo. Parte de la investigación a futuro es comprobar si el tiempo de fase o de tunelaje están directamente relacionados a la variación del coeficiente de transmisión observada en este trabajo.

- Quantum interference effects[22]. Dependiendo del ancho del paquete y su amplitud, este se puede dispersar con el tiempo y esto puede causar interferencia consigo mismo. Conforme diferentes partes del GWP encuentran la barrera de potencial, estos pueden estar interfiriendo, causando fluctuaciones en el coeficiente de transmisión.

Por otro lado, tenemos la transmisión bajo presencia de SOIR (Fig.2).

Se observa una correlación entre las variables: generalmente, a mayor altura de la barrera de potencial ( $Vb$ ) y mayor número de onda inicial ( $k_0$ ), se espera una menor transmisión. Sin embargo, la interacción espín-órbita introduce un comportamiento más complejo. A medida que  $k_0$  aumenta y  $Vb$  disminuye, la transmisión se acerca a 1, indicando una mayor probabilidad de tunelamiento cuántico debido a la SOIR.

Aunque la variación en el coeficiente de transmisión es pequeña (del orden de  $10^{-2}$ ), es significativa y atribuible a la interacción SOIR. Los electrones, con sus diferentes componentes de pseudospin, interactúan, y esta interacción se ve afectada por el número de onda inicial del paquete de ondas gaussiano (GWP), como se observó en estudios previos[1]. Por lo tanto, la SOIR modula la interacción, lo que a su vez causa las fluctuaciones observadas en el coeficiente de transmisión.

#### IV. CONCLUSIONS

In this study, we investigated theoretically and computationally the influence of Rashba spin-orbit interaction (SOIR) on electron transmission across a potential barrier in monolayer graphene. We demonstrated that introducing SOIR significantly modifies electron transmission coefficients, generating complex patterns that are absent in pristine graphene.

An interesting contradiction emerged regarding electron transmission observed in pristine graphene compared to existing literature. While pristine graphene commonly exhibits near-perfect transmission due to suppressed electron backscattering, our results indicated small yet notable transmission reductions. These deviations were attributed to characteristics of the Gaussian wave packet used, specifically quantum interference phenomena, highlighting the sensitivity of electron transport properties to subtle variations in experimental and simulation conditions.

Moreover, the inclusion of rashba SOIR introduced additional small but meaningful variations in transmission coefficients. This effect was closely linked to the interaction between electron pseudo-spin components, influenced distinctly by the direction and magnitude of the initial wave vector. Our observations underscore the delicate yet impactful role pseudo-spin dynamics play in modifying electron transport properties within graphene-based systems.

Future studies could focus on systematically analyzing the relationship between phase time or tunneling times and these observed transmission variations induced by SOIR. Such exploration could offer deeper insights into the quantum mechanical principles governing transport phenomena in graphene and related materials.

Ultimately, our findings highlight the potential of exploiting Rashba spin-orbit interaction to precisely control electron transmission through potential barriers, paving the way toward innovative electronic and spintronic de-

vices, as well as advancing quantum computing technologies.

- 
- [1] E. Serna, I. R. Vargas, R. Pérez-Álvarez, and L. D. Cisneros, *J. Appl. Phys.* **125**, 203902 (2019).
  - [2] W. E. Liu, E. M. Hankiewicz, and D. Culcer, *Materials* **10**, 7 (2017).
  - [3] A. Avsar, J. Y. Tan, T. Taychatanapat, J. Balakrishnan, G. K. W. Koon, Y. Yeo, J. Lahiri, A. Carvalho, A. S. Rodin, E. C. T. O'Farrell, G. Eda, A. H. C. Neto, and B. Özyilmaz, *Nat. Commun.* **5**, 4875 (2014).
  - [4] H. Liu, H. Wang, Z. Peng, J. Jin, Z. Wang, K. Peng, W. Wang, Y. Xu, Y. Wang, Z. Wei, D. Zhang, Y. J. Li, W. Chu, and L. Sun, *Nanoscale Horiz.* **8**, 1235 (2023).
  - [5] E. B. Sonin, *Phys. Rev. B* **79**, 19 (2009).
  - [6] L. Dell'Anna, P. Majari, and M. R. Setare, *J. Phys.: Condens. Matter* **30**, 415301 (2018).
  - [7] B. Trauzettel, D. V. Bulaev, D. Loss, and G. Burkard, *Nat. Phys.* **3**, 192 (2007).
  - [8] A. E. Bernardini, *J. Phys. A.: Math. Theor.* **43**, 489801 (2010).
  - [9] E. Paredes-Rocha, Y. Betancur-Ocampo, N. Szpak, and T. Stegmann, *Phys. Rev. B* **103**, 045404 (2021).
  - [10] Y. Avishai and Y. B. Band, *Phys. Rev. B* **104**, 075414 (2021).
  - [11] D. Shcherbakov, P. Stepanov, and et. al., *Sci. Adv.* **7**, 5 (2021).
  - [12] F. Delkhosh and A. Phirouznia, *Physica E* **66**, 252 (2015).
  - [13] Y. Gindikin and A. Kamenev, *Phys. Rev. B* **111**, 035104 (2025).
  - [14] Y.-T. Yao, S.-Y. Xu, and T.-R. Chang, *Mater. Horiz.* **11**, 3420 (2024).
  - [15] A. K. Geim and K. S. Novoselov, *Nature Mater.* **6**, 183 (2007).
  - [16] R. Cuan and L. Diago-Cisneros, *Rev. Cub. Fis.* **27**, 212 (2010).
  - [17] A. W. López, *Acoplamiento espín-Órbita en heteroestructuras semiconductoras* (2005).
  - [18] A. Carrillo and O. Mendoza, *Geofísica UNAM* (2015).
  - [19] D. W. Horsell, F. V. Tikhonenko, R. V. Gorbachev, and A. K. Savchenko, *Phil. Trans. R. Soc. A* **366**, 245 (2008).
  - [20] A. F. Young and P. Kim, *Nature Phys* **5**, 222 (2009).
  - [21] M. Staelens and F. Marsiglio, *Am. J. Phys.* **89**, 693 (2021).
  - [22] A. Molgado, O. Morales, and J. A. Vallejo, *Rev. Mex. Fis. E* **64**, 1 (2018).